



1 Supraglacial debris thickness variability: Impact on ablation and relation to
2 terrain properties.

3

4 Lindsey I. Nicholson¹, Michael McCarthy^{2,3}, Hamish Pritchard² and Ian Willis³

5 ¹ *Department of Atmospheric and Cryospheric Sciences, Universität Innsbruck, Innsbruck, Austria.*

6 ² *British Antarctic Survey, United Kingdom Research and Innovation, Madingley Road, Cambridge,*
7 *UK*

8 ³ *Scott Polar Research Institute, University of Cambridge, Cambridge, UK*

9 *Correspondence: lindsey.nicholson@uibk.ac.at*

10



11 **ABSTRACT:** *Shallow ground penetrating radar (GPR) surveys are used to characterize the small-*
12 *scale spatial variability of supraglacial debris thickness on a Himalayan glacier. Debris thickness*
13 *varies widely over short spatial scales. Comparison across sites and glaciers suggests that the*
14 *skewness and kurtosis of the debris thickness frequency distribution decrease with increasing*
15 *mean debris thickness, and we hypothesise that this is related to the degree of gravitational*
16 *reworking the debris cover has undergone, and is therefore a proxy for the maturity of surface*
17 *debris covers. In the cases tested here, using a single mean debris thickness value instead of*
18 *accounting for the observed small-scale debris thickness variability underestimates modelled*
19 *midsummer sub-debris ablation rates by 11-30 %. While no simple relationship is found between*
20 *measured debris thickness and morphometric terrain parameters, analysis of the GPR data in*
21 *conjunction with high-resolution terrain models provides some insight to the processes of debris*
22 *gravitational reworking. Periodic sliding failure of the debris, rather than progressive mass*
23 *diffusion, appears to be the main process redistributing supraglacial debris. The incidence of*
24 *sliding is controlled by slope, aspect, upstream catchment area and debris thickness via their*
25 *impacts on predisposition to slope failure and meltwater availability at the debris-ice interface.*
26 *Slope stability modelling suggests that the percentage of the debris-covered glacier surface area*
27 *subject to debris instability can be considerable at glacier scale, indicating that up to 22% of the*
28 *debris covered area is susceptible to developing ablation hotspots associated with patches of*
29 *thinner debris.*



30 1. Introduction

31 Debris-covered glaciers are the dominant form of glaciation in the Himalaya (e.g. Kraaijenbrink
32 et al. 2017), and are common in other tectonically active mountain ranges worldwide (Benn et
33 al. 2003). Supraglacial debris cover alters the rate at which underlying ice melts in comparison
34 to clean ice in a manner primarily governed by the thickness of the debris cover (e.g. Østrem,
35 1959; Loomis, 1970; Mattson et al., 1992; Kayastha et al. 2000; Nicholson and Benn, 2006; Reid
36 and Brock, 2010): A thin supraglacial debris cover (< a few cm) enhances melt, while thicker
37 debris cover reduces melt by insulating the ice beneath from surface energy receipts. Prevailing
38 weather conditions, and local debris properties, such as albedo, lithology, texture and moisture
39 content, also influence the amount of energy available for sub-debris ablation, and modify the
40 exact relationship between debris thickness and ablation rate, but the general characteristics of
41 the so-called Østrem curve are robust, further demonstrating the dominant role of debris
42 thickness in this relationship (Fig. 1).

43 Both theory and observations indicate that the spatial variability of supraglacial debris
44 thickness typically has both a systematic and a non-systematic component. Debris thickness
45 tends to increase towards the glacier margins and terminus due to concentration by
46 decelerating ice velocity, and increasing background meltout rate (e.g. Kirkbride, 2000). This
47 systematic variation is evident in field measurements of debris cover thickness (e.g. Zhang et al.,
48 2011), and in characterizations of debris thickness as a function of the surface temperature
49 distribution observed from satellite imagery (e.g. Mihalcea et al. 2006; Mihalcea et al. 2008a;
50 Mihalcea et al. 2008b; Foster et al. 2012; Rounce and McKinney, 2014; Schauwecker et al. 2015;
51 Gibson et al. 2017). At local scales, debris thickness varies less systematically according to the
52 input distribution, local meltout patterns and gravitational and meltwater reworking of the
53 supraglacial debris. Manual excavations (e.g. Reid et al., 2012), observations of debris thickness
54 made above exposed ice cliffs (e.g. Nicholson and Benn, 2012; Nicholson and Mertes 2017), and
55 debris thickness surveyed by ground penetrating radar (McCarthy et al., 2017) demonstrate
56 that debris thickness varies considerably over short horizontal distances. Thus, the thickness of
57 debris over a sampled area of glacier surface is better expressed as a probability density
58 function than a single value (e.g. Nicholson and Benn, 2012; Reid et al., 2012).

59 Exposed ice faces within debris-covered glacier ablation areas are known to contribute
60 disproportionately to glacier ablation compared to their area (e.g. Sakai et al., 2000; Juen et al.,
61 2014; Buri et al., 2016; Thompson et al., 2016), and it has been proposed that such 'ablation
62 hotspots', along with stagnation, are the reasons for the observed similarity in surface lowering
63 rates of otherwise comparable clean and debris-covered ice surfaces (e.g. Kääb et al., 2012,
64 Nuimura et al., 2012). Given the strongly non-linear relationship between ablation rate and
65 debris thickness (Fig. 1), patches of thinner debris within a generally thicker supraglacial debris
66 cover can similarly be expected to contribute disproportionately to glacier ablation, but this has
67 only rarely been considered (Reid et al., 2012). The implication of this would be that
68 calculations of sub-debris ice ablation rate and meltwater production using spatially-averaged
69 mean debris thickness may differ substantially from the actual meltwater generated from a
70 debris layer of highly variable thickness within the same area. Therefore, there remains a
71 critical need to be able to quantify not only mean supraglacial debris thickness, but also local
72 debris thickness variability, in order to understand how debris cover is likely to impact glacier



73 behaviour, meltwater production and contribution to local hydrological resources and global
74 sea level rise.

75 Meeting this need requires a better understanding of debris thickness variability and the
76 controls upon it, ideally by means of more readily observable properties. Topographic data
77 has been used to predict soil thickness on hilly, extraglacial terrain under the assumption of
78 steady state conditions (e.g. Pelletier and Rasmussen, 2009). However, associated soil thickness
79 relationships as a function of slope curvature (Heimsmath et al., 2017) are based on progressive
80 creep processes, while reworking of supraglacial debris cover occurs mainly as a result of
81 gravitational instabilities such as 'topples, slides and flows' (Moore, 2017). Nevertheless, as the
82 debris thickness that can be supported on a slope is related to slope angle, debris texture and
83 saturation conditions (Moore, 2017) it might still be possible to find explicit relationships
84 between topography and debris thickness. If high-resolution topography data, which is
85 increasingly widely available, could be used to indicate local debris thickness variability, such
86 information would complement spatially averaged mean supraglacial debris thickness values
87 derived by other methods (cf. Arthern et al. 2006).

88

89 **2. Aim of the study**

90 This study investigates the evidence for small-scale debris thickness variability, assesses the
91 impact of local debris thickness variability on calculated sub-debris ice ablation rates, and
92 explores the potential for predicting local debris thickness variability from morphometric
93 terrain parameters. First, debris thickness data from shallow ground penetrating radar surveys
94 are used to characterize the small-scale spatial variability of debris thickness on a Himalayan
95 glacier, examine evidence of gravitational reworking processes and compare the observed
96 variability to previously published data. Second, the impact of the observed small-scale debris
97 thickness variability on modelled sub-debris ablation rates is assessed. Third, a
98 contemporaneous high resolution terrain model and optical imagery are employed to determine
99 if the observed thickness variability can be predicted from more readily measured surface
100 terrain properties. Finally, a slope stability model is calibrated with the GPR and ablation model
101 data and used to determine the percentage of our study areas in the debris-covered ablation
102 zone that are subject to debris instability, and potentially the formation of ablation hotspots, in
103 mid-ablation season (August) conditions.

104

105 **3. Study site and data**

106 The Ngozumpa glacier is a large dendritic debris-covered glacier of the Eastern Himalaya,
107 located in the upper Dudh Kosi catchment, Khumbu Himal, Nepal (Fig. 2a). The glacier has a
108 total area of 61 km² of which the lower 22 km² is heavily debris-covered, with hummocky
109 surface relief in the order of 50m over distances of 100m (Fig 2b), studded with supraglacial
110 ponds and exposed ice cliffs (Benn et al., 2001). The NE and E branches are no longer connected
111 dynamically to the main trunk (Thompson et al., 2016), which is fed solely by the W branch
112 descending from the flanks of Cho Oyu (8188 m). The southernmost 6.5 km of the glacier is
113 nearly stagnant (Quincey et al. 2009) and has a low surface slope of ~4°. The terrain of this
114 glacier, its wasting processes and the evolution of surface lakes have been well studied through



115 a series of previous publications (Benn et al., 2000 & 2001; Thompson et al., 2012 & 2016), as
116 have the debris properties including limited measurements of debris thickness (Nicholson and
117 Benn, 2012).

118 Debris thickness over much of the debris-covered area is in excess of 1.0 m precluding
119 widespread manual excavation. However, in 2001 measurements of debris thicknesses exposed
120 above ice cliffs were made by theodolite survey at ~1 and 7 km from the terminus (Nicholson
121 and Benn, 2012). These data provided only coarse estimates of debris thickness as neither the
122 slope angle of the debris exposure, nor the impact of the theodolite bearing angle were
123 accounted for in the vertical offsetting used to obtain the debris thickness. In April 2016
124 terrestrial photogrammetry was used to create a high resolution scaled model of the local
125 glacier surface from which debris thickness estimates were made in a manner analogous to the
126 theodolite survey at a location ~2 km from the terminus near Gokyo village (Nicholson and
127 Mertes, 2017). At the same time, several GPR surveys, totalling 3301 m, were undertaken in this
128 area and a single 238 m GPR survey was done close to the glacier margin ~1 km from the glacier
129 terminus (Fig. 2a). Meteorological data are not available from the Ngozumpa glacier surface at
130 this site, so the ablation model was forced using several years of meteorological data measured
131 at the Pyramid weather station (27.95° N / 86.81°E, 5035 m a.s.l.) operated by the Ev-K2-CNR
132 consortium (<http://www.ev-k2-cnr.org/cms/en>) in the neighbouring valley. A digital terrain
133 model generated from Pleiades tri-stereo imagery acquired in April 2016 is used to relate the
134 measured debris thicknesses to the glacier surface terrain.

135

136 **4. Methods**

137

138 4.1 GPR debris thickness data collection and processing

139 GPR measurements were made between 31st March and 20th April 2016 broadly following the
140 methods of McCarthy et al. (2017). Debris thickness was sampled in 36 individual radar
141 transects, covering sloping and level terrain with coarse and fine surface material. The GPR
142 system was a dual frequency 200/600MHz IDS RIS One, mounted on a small plastic sled and
143 drawn along the surface. Data were collected to a Lenovo Thinkpad using the IDS K2 FastWave
144 software. This system produces two simultaneous radargrams for each acquisition. The 200
145 and 600MHz antennas have separation distances of 0.230 m and 0.096 m respectively. Data
146 acquisition used a continuous step size, a time window of 100 ms and a digitization interval of
147 0.024 ns. The location of the GPR system was recorded simultaneously at 1 s intervals by a low
148 precision GPS integrated with the IDS which assigns a GPS location and time directly to every
149 twelfth GPR trace, and by a more accurate differential GPS (dGPS) system consisting of a
150 Trimble XH and Tornado antenna mounted on the GPR and a local base station of a Trimble
151 Geo7X and Zephyr antenna.

152 Radargrams were processed in REFLEXW (Sandmeier software) by applying the steps shown in
153 Table 1. The reflection at the ice surface was picked manually wherever it was clearly
154 identifiable and was not picked if it was indistinct. The appropriate signal velocity for the
155 supraglacial debris was obtained by burying a 1.5 m long steel bar to a known depth and then
156 passing the GPR over the buried target and picking the two-way travel time to its reflection (Fig.



157 3 a and b). Both fine and coarse material gave similar wave speeds (0.15 and 0.16 m ns⁻¹). These
158 were averaged to obtain a bulk value that is considered representative for all the radar lines
159 measured and is comparable to values from the debris-covered Lirung glacier, central Nepal
160 (McCarthy et al., 2017). Debris thickness was calculated using ice surface two-way travel times
161 and the mean of the two wave speed measurements (0.16 m ns⁻¹), taking the geometry of the
162 GPR system into account. Uncertainties were propagated according to McCarthy et al (2017)
163 and range from 0.14 - 0.83 m, generally increasing with debris thickness.

164 During processing, the integrated GPS locations (typical accuracy of ~ 3 m) were substituted for
165 dGPS locations (typical post-processed accuracy of < 0.05 m) by matching GPS and dGPS
166 timestamps. Where differential correction was not possible due to a lack of visible satellites, the
167 integrated GPS locations were used. The locations of GPR data collected between timestamps
168 were interpolated linearly in REFLEXW. Where the ice surface was identifiable in radargrams of
169 both frequencies, the measurement made using the higher frequency was assigned because
170 higher frequencies give higher precision. GPR data quality was assessed by comparing debris
171 thicknesses calculated using picks from the two different frequencies in the same location (Fig.
172 3c) and by comparing debris thicknesses at transect crossover points (Fig. 3d). In both cases,
173 points fit well to the 1:1 line. To show how debris thickness varies with topography, radargrams
174 were topographically corrected for display purposes after the ice interface had been picked.

175 4.2 Ablation modelling

176 In the absence of suitable field measurements of sub-debris ice ablation, a model of ice ablation
177 beneath a debris cover was applied to assess the impact of debris thickness variability on
178 calculated ablation rates. As recent, high quality, local meteorological data are not available to
179 force a time-evolving numerical model, typical ablation season conditions measured at the
180 nearby Pyramid weather station were used to force a steady-state model of sub-debris ice
181 ablation that has been previously published and evaluated against field data (Evatt et al., 2015).

182 Ice ablation conditions are generally restricted to the summer months in the eastern Nepalese
183 Himalaya (Wagnon et al., 2013). For the illustrative simulations performed here, the model was
184 forced with mean August meteorological conditions from 2003-2009 ($< 2\%$ of August hourly
185 data are missing), and assuming the ice temperature to be 0°C . This provides forcing variables
186 of air temperature (3.27°C), incoming shortwave (208 Wm⁻²) and longwave (314 Wm⁻²)
187 radiation, wind speed (1.94 ms⁻¹) and relative humidity (97%). Appropriate debris properties
188 for dry debris in summer time on the Ngozumpa glacier were adopted from Nicholson and Benn
189 (2012), whereby debris properties of effective thermal conductivity, dry surface albedo and
190 porosity were taken to be 1.29 Wm⁻¹ K⁻¹, 0.2 and 0.3 respectively. Ice albedo, debris thermal
191 emissivity and the debris surface roughness length, friction velocity and exponential decay rate
192 of wind were adopted from Evatt et al. (2015).

193 The model is used to generate an Østrem curve and associated surface debris temperature for
194 the stated inputs, as a function of debris thickness. The model does not account for variability in
195 surface energy receipts due to local or surrounding terrain, or the effects of spatially or
196 temporally variable debris properties other than thickness, and the chosen input properties are
197 only approximate. However, this does not preclude its illustrative use in investigating the
198 influence of variable debris thickness on calculated ablation rate. Modelling was carried out for



199 three sites for which local debris thickness data is available: (i) the margin study area ~1km
200 from the glacier terminus, (ii) the main Gokyo study area ~2 km from the terminus, both
201 measured by GPR in 2016, and (iii) the upglacier study area ~7 km from the terminus,
202 measured by theodolite survey in 2001 (Fig 2). Ablation rate and surface temperature is
203 calculated for the mean debris thickness is compared to that yielded by multiplying the
204 percentage frequency distribution of debris thickness with the modelled Østrem and surface
205 temperature curves. Ablation totals for the month of August are calculated and that derived
206 using the mean debris thickness value is expressed as a percentage deviation of that derived
207 using locally variable debris thickness. Used in this form we assume the model itself to be error
208 free. To isolate the error associated with debris thickness, all other model inputs are also
209 assumed to be error free. Each GPR debris thickness has an associated error, but as no
210 quantified error assessment is available for the thickness values measured by theodolite at 7 km
211 from the terminus a fixed error of ± 0.15 m was applied to these data. The model was run with
212 maximum and minimum debris thickness values according to the assigned errors, to provide an
213 indication of uncertainty of the reported percentage difference in monthly total ablation.

214 4.3 Terrain analysis

215 In order to assess the static relationship between the debris distribution and terrain properties,
216 we used a 5 m resolution digital terrain model (DTM) derived from Pléiades optical tri-stereo
217 imagery taken during the field campaign on the 12th April 2016. The DTM was generated from
218 photogrammetric point clouds extracted from the Pléiades imagery, using a semi-global
219 matching (SGM) algorithm (Hirschmüller, 2008) within the IMAGINE photogrammetry suite of
220 ERDAS IMAGINE. The three images of each triplet were imported and the rational polynomial
221 coefficients (RPC) provided with the Pléiades data were used to define the initial functions for
222 transforming the sensor geometry to image geometry. With those transformation functions,
223 individual geometries of each image in the triplet were orientated relative to each other. To
224 obtain the most accurate exterior orientation possible, initial RPC functions were refined using
225 automatically-extracted tie points. The calculated point clouds were then filtered for outliers,
226 mainly found in very steep and shaded areas, using local topographic 3D filters applied in SAGA
227 GIS software, and converted into a 5 m-resolution DTM using the average elevation of all points
228 within one raster cell as the elevation value for the cell. Gaps were present in very steep areas,
229 where there was cloud, and in areas with low contrast because of fresh snow or liquid water.

230 Terrain properties were extracted using the ArcGIS tools Slope, Aspect and Curvature. GPR data
231 were resampled to the same resolution as these rasters (5 m) by taking the mean of the
232 measurements that occurred within each pixel. This was done using the Point to Raster tool in
233 ArcGIS. GPR data within 5 m of ice cliffs were excluded for comparisons made between debris
234 thickness and topography, in order that their slope, aspect and curvature were not
235 misrepresented. Similarly, GPR data for which dGPS locations were not available were excluded
236 due to their lack of positional accuracy.

237 Ponded water at the surface is associated with the deposition of layers of fine sediments and
238 rapid sedimentation by marginal slumping (Mertes et al., 2017). The recent history of ponded
239 water on the parts of the glacier surface sampled by the radar transects was mapped using air
240 photographs from 1984, and seven cloud-free optical satellite images spanning 2008-2016.



241 These images consisted of six Digital Globe images, one CNES/Astrium image, all obtained via
242 Google Earth, and the optical image from the 2016 Pleiades acquisition used to generate the
243 DTM.

244 4.4 Slope stability modelling and classification

245 Slope stability modeling was carried out following Moore (2017). For the three study areas
246 shown in Fig. 2, debris was classified as either stable or unstable. Unstable debris was further
247 classified as being unstable due to:

- 248 1. Oversteepening, where surface slope exceeds the debris-ice interface friction coefficient,
- 249 2. Saturation excess, where the modeled water table height is greater than the debris
250 thickness, and
- 251 3. Meltwater weakening, where the modeled water table height is less than the debris
252 thickness, but debris pore pressures are sufficiently raised to cause instability.

253 Surface slope (see Section 4.3), modeled midsummer ablation rate (see Section 4.2), upstream
254 contributing area, and mean debris thickness (see Section 4.1) were used as inputs to the
255 model. Upstream contributing area was determined from the DTM in ArcGIS using the Flow
256 Direction and Flow Accumulation tools. Sinks in the DTM were filled if they were less than 3 m
257 deep, following Miles et al (2017), using the ArcGIS Sink and Fill tools. Surface water flowpaths
258 were also determined using the Stream To Feature tool.

259 The model also requires input values for the debris-ice interface friction coefficient, the
260 densities of water and wet debris, and the saturated hydraulic conductivity of the debris. A
261 value of 0.5 was used for the debris-ice interface friction coefficient, following Barrette and
262 Timco (2008) and Moore (2017). Values of 1000 and 2190 kg m⁻³ were used for the densities of
263 water and wet debris, respectively, where wet debris was assumed to have a porosity of 0.3,
264 after Conway and Rasmussen (2000), and the density of rock was assumed to be 2700 kg m⁻³
265 after Nicholson and Benn (2006). The saturated hydraulic conductivity of the debris, which is
266 the parameter around which there is most uncertainty, was determined using the GPR data.
267 Sections of the GPR transects, and subsequently their corresponding DTM pixels, were defined,
268 by visual inspection on the basis of the debris morphology, as either stable or unstable. Sections
269 of thin debris on steep slopes were considered to be unstable if they occurred among sections of
270 thick debris on shallow slopes. Sections of anything not considered to be unstable were
271 considered to be stable. Debris stability was then modeled for the same DTM pixels using a wide
272 range of conductivity values. The conductivity value that minimized the difference between the
273 number of pixels that were modeled and observed as being stable or unstable was considered to
274 be optimal. Minimization was carried out using ROC analysis, following Fawcett (2006) and
275 Herreid and Pellicciotti (2017). The resulting saturated hydraulic conductivity value of 40 m d⁻¹
276 is well within the expected range of 10⁻⁷-10³ m d⁻¹ (Fetter, 1994), and is consistent with the
277 debris being well-drained.

278 The percentage areal coverage of debris instability was calculated for each of the three study
279 areas (Fig. 2). This was done both including and excluding ice cliffs and ponds, where ice cliffs
280 and ponds were manually digitized from the orthophoto associated with the DTM.



281 The GPR data, DTM and associated orthophoto were collected in March/April 2016, while slope
282 stability modeling was carried out using midsummer (August) ablation rates. It is likely that the
283 debris on a given slope becomes more or less stable seasonally with changes in ablation rates.
284 However, GPR observations of debris instability in March/April are likely to be representative
285 of midsummer debris instability for saturated hydraulic conductivity as maximum melt is
286 expected in midsummer. Similarly, while pond incidence and area vary seasonally on Himalayan
287 glaciers, recurrence rates are generally high (Miles et al., 2016), so manually digitized ponds and
288 ice cliffs for March/April are assumed to be broadly representative of ponds and ice cliffs in
289 midsummer for percentage area debris instability calculations excluding ponds and ice cliffs.
290 Finally, model results should be treated only as a best approximation because the model
291 assumes debris thickness and ablation rate are spatially homogeneous in each study area,
292 which, as discussed by Moore (2017), is clearly not the case.

293 5. Results and discussion

294

295 5.1 GPR debris thickness and variability

296 The quality of the GPR data is generally high. The ice surface was clearly identifiable through the
297 debris in the majority of the radargrams collected. This is likely because the GPR system was
298 used in ‘continuous-mode’ and appropriate acquisition parameters were used. For those
299 radargrams in which the ice surface was not easily identifiable, the debris was generally too
300 thick. This means there is the possibility of a slight thin bias in the data. However, penetration
301 depth was often greater than 7 m, which is likely near the maximum debris thickness. Debris
302 thickness was found to be highly variable with a total range of 0.18 to 7.34 m (Fig. 4 and
303 examples in Fig 5). There is coherent structure to the debris thickness variation along transects
304 (Fig. 4): In some areas, changes in debris thickness along the transect are gradual, while in a
305 number of cases, there are abrupt changes in debris thickness along a transect associated with
306 pinning points or topographic hollows and cavities in the underlying ice, which the debris cover
307 fills (see Section 5.3 and Fig. 6).

308 Simple statistics of the debris thickness derived from the GPR samples of this study compared
309 with debris thickness datasets available from other glaciers are given in Table 2. Mean debris
310 thickness measured by GPR towards the glacier margin is thicker, and shows wider spread and
311 lower skewness and kurtosis, than the GPR thickness data collected at the Gokyo study area
312 (Table 2; Fig. 4; Fig 5a-c). The percentage frequency histogram of GPR debris thickness from the
313 glacier margin has a similar shape, but a positive offset compared to data obtained by surveying
314 of ice faces about 1 km from the glacier terminus in 2001, while the GPR data from Gokyo agrees
315 closely with the estimates of debris thickness from the photographic terrain model (Nicholson
316 and Mertes, 2017). The 2001 surveyed debris thickness data from further upglacier (Nicholson
317 and Benn, 2012) is thinner, more skewed, and has higher kurtosis than the sites further
318 downglacier (Fig. 5a-c).

319 Clearly, while debris thickness shows small-scale variability in all cases on the Ngozumpa
320 glacier, the details of that variability differ from site to site. This is also observed when
321 considering data from other glaciers (Table 2; Fig. 5). Debris thickness at the Lirung glacier,
322 central Nepal shows a bimodal distribution not replicated at the other sites. This is suspected to



323 be due at least partly to sampling bias, as the measurements were made to test the GPR method
324 rather than to characterize typical debris thickness at this glacier. At Suldenferner, in the Italian
325 Alps, debris thickness measured across the whole debris-covered area by excavation, and along
326 cross- and down-glacier transects by GPR, shows a substantially thinner mean than the
327 Himalayan cases, with greater skewness and kurtosis. The debris cover on the medial moraine
328 of Haut Glacier d’Arolla in the Swiss Alps is even thinner with yet more pronounced skewness
329 and kurtosis. Thus, debris thickness variability at the Alpine sites shown here is more
330 comparable to that of the upper Ngozumpa, while the Lirung glacier measurements appear
331 broadly more similar to sites further downglacier on the Ngozumpa glacier.

332 The medial moraine on Haut Glacier d’Arolla emerged during glacial recession in the second half
333 of the 20th century (Reid et al., 2012), offering an example of a recently developed debris cover.
334 The debris-covered part of Suldenferner developed its continuous debris cover since the
335 beginning of the 19th century, when the glacier was mapped with debris cover below ~2500 m
336 and only surficial medial moraine bands extending up to 2700 m (Finsterwalder and Lagally,
337 1913). The Nepalese glaciers are thought to have been debris-covered for longer (Rowan,
338 2016), although it remains unclear when their debris covers first developed.

339 The percentage frequency distributions shown in Fig. 5, viewed in the context of the relative
340 ‘maturity’ of the debris covers sampled, are suggestive of a progressive change in skewness and
341 kurtosis debris thickness variability over time, as debris accumulates and undergoes
342 progressively more gravitational reworking. The more mature debris covers on the Ngozumpa
343 and Lirung glaciers is generally thick and characterised by hummocky terrain (cf. Fig. 2b),
344 dissected with ponds and ice faces, whereas, the less mature debris cover on Suldenferner is
345 generally thinner and the terrain is less hummocky, with relief primarily associated with
346 incision by supraglacial streams. Similarly, the observed progressive change in thickness and
347 skewness/kurtosis of the debris sites downglacier on the Ngozumpa glacier would reflect the
348 downglacier increase in maturity of the debris covered surface.

349 *5.2 Ablation modelling using mean and variable debris thickness*

350 Ablation was calculated for three locations on the Ngozumpa glacier (Fig. 2) encompassing
351 different mean debris thickness and debris thickness variability (Fig. 5; Fig. 6a), that might
352 reflect different stages in debris cover maturity (see Section 5.1), but it should be noted that the
353 sampling method and sample number differs between locations (Table 2).

354 The ablation calculated for typical August conditions using the mean debris thickness for each
355 location on the glacier totalled 0.07, 0.11 and 0.32 m of ice surface lowering over the month at
356 the 1, 2 and 7 km sites respectively. This agrees with the general expected patterns of ablation
357 gradient reversal towards the terminus of a debris-covered glacier (e.g. Benn and Lehmkuhl,
358 2000; Bolch et al., 2008; Benn et al., 2017). Accounting for the percentage frequency
359 distribution of debris thickness increased the monthly total surface lowering due to ablation to
360 0.08, 0.16 and 0.46 m, at 1, 3 and 7 km respectively. In these illustrative example, using a mean
361 debris thickness instead of the local frequency distribution of debris thickness, underestimates
362 the ablation rate at these sites by 11-30 % over a month of typical August conditions (Fig 6c).
363 These values are specific to the cases presented here but can be considered indicative of the
364 order or the effect of using mean debris thickness instead of the local variable debris thickness.



365 Considering the maximum and minimum error bounds of the debris thickness distribution (Fig
366 6a and c) increases the range of this underestimate to 10-40%. This suggests that local mean
367 debris thickness, and also other measures of central tendency (tested but not shown), are likely
368 to be poor metrics for ablation modelling for typical debris cover. Instead, sufficient data points
369 of debris thickness to capture the local variability are likely to give a more reliable ablation
370 estimate from model simulations. As the melt rate in the ‘thin debris’ part of the Østrem curve
371 responds more sensitively to changes in debris thickness than it does in the ‘thick debris’ part of
372 the curve, the impact of accounting for local spatial variability in debris thickness varies
373 inversely with debris thickness (Fig 6c). This is compounded by the fact that thinner debris
374 appears to have more skewness and kurtosis in the percentage frequency distribution of debris
375 thickness, meaning that the offset between the calculated mean debris thickness and the typical
376 debris thickness is likely to be greater.

377 Highly variable debris thickness can be expected to impact methods of mapping debris
378 thickness using thermal-band satellite imagery, as our data show that the debris thickness
379 variability within individual pixels of a thermal-band satellite image may be large. The modelled
380 surface temperature for mean August conditions was 19.5, 19.0 and 16.6°C for the mean debris
381 thickness at the margin, Gokyo and upglacier study areas respectively. Accounting for the local
382 debris variability at the lowest site altered the calculated surface temperature by < 0.1°C, and, at
383 the middle and upper locations, reduced the calculated surface temperatures by 0.5 and 1.5°C
384 respectively (Fig 6d). This highlights the manner in which variable debris thickness can be
385 expected to influence the pixel values in satellite thermal imagery, whereby a mean debris
386 thickness calculated from a pixel temperature can be expected to underestimate the true mean
387 debris thickness.

388 *5.3 Relationships between debris thickness and terrain properties*

389 Visual inspection of the radargrams indicates that the thinnest debris cover occurs on steep
390 slopes (Fig. 7a and b). On the basis that slope failure typically redistributes mass from areas of
391 high slope angle, and that debris sliding was often experienced while collecting the GPR data, it
392 seems likely that this is the result of high debris export rates in these areas due to frequent or
393 recent slope failure in the form of sliding events (c.f. Lawson, 1979, Heimsath et al. 2012). Here,
394 the debris surface is approximately parallel to the ice surface, and this appears to be a
395 characteristic of debris covers at or near the limits of gravitational instability. Localized areas of
396 thick debris are found below steep slope sections in the form of infilled ice-surface depressions.
397 Modelled surface flowpaths (Fig. 7b) cross-cut the GPR transects where these depressions are
398 located, indicating that they were likely incised by meltwater. This suggests that meltwater is
399 transported in sub-debris supraglacial channels (c.f. Miles et al. 2017), but also that meltwater
400 routing is a local control on debris thickness by providing topographic lows that become infilled
401 by debris. Additionally, it seems likely that meltwater channels undercut steep slopes, thereby
402 causing debris failure. Steep slopes on debris-covered glaciers are relatively short, so
403 undercutting would have the combined effect of increasing slope angle and also reducing the
404 confining force (or buttressing effect) imparted by down-slope debris cover. In some places,
405 thick debris is contained behind pinning points of the underlying ice (Fig. 7a and b), which
406 results in the occurrence of talus slopes (Fig. 7a), this stabilizes the debris and increases the



407 confining force. Thick debris on convex, divergent terrain provides evidence of topographic
408 inversion due to differential ablation (Fig. 7c).

409 The single glacier margin transect shows increasing debris thickness towards the glacier margin
410 (Fig. 4b and Fig. 7e). This is expected as a result of: (i) material delivered onto the glacier from
411 the inner flanks of the lateral moraines as they are progressively debutressed by glacier surface
412 lowering; and (ii) lower surface velocities at the glacier margins, hence slower debris advection
413 rates. The Ngozumpa glacier and others in the region typically have troughs at the boundary
414 between the glacier and the lateral moraine, and evidence of thicker debris here reinforces the
415 idea that these troughs are eroded by meltwater routed along the glacier margins (Benn et al.,
416 2017).

417 Since 1984, the development of supraglacial ponds within the Gokyo study area is likely to have
418 affected two areas of radar transects: Several transects towards the north of the Gokyo study
419 area, which were partially affected by lakes in 2012 and 2014, and a single transect towards the
420 east of the Gokyo study area, which was partially affected by lakes in all the sampled years
421 except 2014 and 2016 (Fig. 4). One of the transects towards the north of the Gokyo study area
422 shows thick debris and some internal structures (Fig. 7e) including what may be a relict slump
423 structure, where a package of sediment fell into the lake from its margin as the lake expanded
424 (e.g. Mertes et al. 2016). Thick debris in former supraglacial lakes is likely due to high
425 sedimentation rates in the ponds and by slumping at lake margins during lake expansion
426 (Mertes et al. 2016). Modelling suggests that subaqueous sub-debris melt rates are low (Miles et
427 al. 2016), so debris thickening caused by the melt-out of englacial debris is likely to be minimal.
428 The radar stratigraphy over former lake beds suggests multiple near surface reflectors that can
429 reasonably be interpreted as fine lake sediments overlying coarser supraglacial diamict,
430 suggesting that the locally thicker sediments associated with lakes are due to deposition from
431 sediment-rich supraglacial and englacial meltwaters flowing into a more sluggishly circulating
432 pond.

433 The debris thickness sampled with GPR in this study does not show distinct relations with slope,
434 aspect or curvature (Fig. 8a, b, c). Binning the thickness data with respect to slope indicates a
435 step decrease in debris thickness above surface slope angles of around 20-23° (Fig. 8a). This
436 may represent a transition from the low debris transport rates expected on low-gradient, stable
437 slopes, to the high-debris transport rates expected on steep, failure-prone slopes. While slope
438 and curvature are relatively evenly sampled by the dataset, the same is not true for aspect.
439 While southerly and north-easterly aspects are well sampled, samples are scarce in other aspect
440 sectors, rendering interpretation of potential aspect controls on debris thickness difficult (Fig
441 8e). Tentatively, our data suggests thin debris is scarcer for northwesterly aspects, than others
442 (Fig. 8b, e). Comparing the GPR measurements with both slope and aspect simultaneously (Fig.
443 8e) shows what would be expected from Fig. 8a and 8b: That debris tends to be thicker on
444 northwest facing slopes, and thinner on steeper slopes away from the north-westerly sector.
445 During the pre-monsoon in the Himalaya, more melting is likely to occur on southeast-facing
446 slopes than southwest-facing slopes because clouds often reduce incoming shortwave radiation
447 in the afternoon (e.g. Kurosaki and Kimura, 2002; Bhatt and Nakamura, 2005, Shea et al., 2015).
448 This effect is observable in global radiation data (Fig. 8d). Distributing incoming shortwave
449 radiation on slopes of different slopes and aspects reveals the northwest sector to be the one



450 receiving least solar radiation in midsummer conditions (Fig. 8f). As a result slopes in this sector
451 may be expected to produce less meltwater meaning that debris water content, pore pressure
452 remain low, maintaining higher shear strength and greater stability, allowing thicker debris to
453 be sustained even on steep slopes (Moore, 2017). Samples from steep slopes in the south-east
454 sector are scarce, likely due to the higher melt rates resulting from higher solar radiation
455 receipts, serving to reduce slope angles here (Buri and Pellicotti, 2018). As a result of the
456 absence of steep slopes in the southeast sector, minimum debris thicknesses are displaced to
457 steeper slope angles flanking the aspect sector or highest midsummer solar radiation receipts.
458 No significant correlations were found between surface curvature and debris thickness (Fig. 8c),
459 but perhaps this is to be expected, as the GPR samples only a snapshot of a dynamically evolving
460 surface. Depending on the stage of topographic inversion sampled, thicker debris could be
461 found at the hummock summit or in the surrounding troughs. Furthermore, the predominance
462 of slope failure over slope creep mechanisms of gravitational reworking would serve to mask
463 any existing relationship with curvature. Ultimately, it seems that the relationship between
464 debris thickness and morphometric terrain parameters (slope, aspect and curvature) is
465 complex.

466 *5.4 Slope stability modelling*

467 Slope stability modelling suggests that, under mid-August ablation conditions, the percentage of
468 the debris-covered area interpreted as potentially unstable for the three study areas of
469 Ngozumpa Glacier is between 13 and 34% including ponds and ice cliffs, and between 12 and
470 22% if ponds and ice cliffs are excluded (Fig. 9). The percentage of potentially unstable surface
471 area increases upglacier, as debris thickness decreases and ablation rates increase (Fig 6c).
472 Oversteepening was found to be the dominant cause of instability in all three study areas,
473 meaning that the debris is most likely to be unstable where surface slope is greater than $\sim 27^\circ$
474 (i.e. greater than the inverse tangent of the debris-ice interface friction coefficient). In the Gokyo
475 and upglacier study areas, saturation excess was found to be the second most important cause
476 of instability and meltwater weakening the third. Here, it seems that the debris is thin enough
477 and ablation rates high enough for the debris to become saturated with surface meltwater. In
478 the downglacier margin study area, however, meltwater weakening was found to be more
479 important than saturation excess, presumably because the debris here is considerably thicker
480 and ablation rates providing meltwater are lower.

481 On the basis that thin debris is more likely to exist on unstable slopes, or on slopes that have
482 recently failed, and that debris-covered glaciers typically extend to lower elevations than
483 debris-free glaciers, these results have important implications for debris-covered glacier surface
484 mass balance. Debris gravitational instability provides a mechanism by which relatively large
485 parts of debris-covered glaciers can experience high melt rates, even if debris is generally thick.

486

487 **6. Conclusions**

488 Debris thickness is known to vary over the surfaces of debris-covered glaciers due to advection,
489 rockfall from valley sides, movement by meltwater, and slow cycles of topographic inversion.
490 The debris thickness data presented here suggest that the local debris thickness variability may



491 show characteristic changes in skewness and kurtosis associated with progressive thickening
492 and/or reworking of debris cover over time. On this basis the likely distribution of debris
493 thickness might be predicted by the maturity, or time elapsed since development, of the debris
494 cover found on a glacier surface.

495 For the thickly debris-covered glaciers of the Himalaya, sub-debris melt rates across the
496 ablation zones are generally considered to be small compared to sub-aerial melt rates at ice
497 cliffs (e.g. up to 5 cm d⁻¹, Watson et al. 2016) and sub-aqueous bare ice melt rates at supraglacial
498 lakes (e.g. 2-4 cm d⁻¹, Miles et al. 2016). Our GPR data confirm that the debris cover on
499 Ngozumpa Glacier is typically thick, with the thickest debris found on shallower slopes or the
500 sites of former supraglacial ponds. Here, the debris is too thick for the daily temperature wave
501 to penetrate to the ice (Nicholson and Benn, 2012). Consequently, even in core ablation season
502 conditions, typical melt rates are low across most of the debris covered area. However,
503 processes of debris destabilization can form areas of thin debris within thicker debris. These
504 areas of thinner debris skew the spatially-averaged ablation rate in a manner that is analogous
505 to that caused by exposed ice faces. Here, sub-debris melt rates under thinner debris are
506 expected to be significantly above average, and even comparable with bare ice melt rates
507 further upglacier. We find that using mean debris thickness values in surface mass balance
508 models is likely to cause melt to be underestimated, and our results confirm previous
509 suggestions that debris thickness is better represented in surface mass balance models as a
510 probability density function (e.g. Nicholson and Benn, 2012; Reid et al., 2012).

511 On the surface of the Ngozumpa glacier, our data suggest that topography is an important
512 additional local control on debris thickness distribution, via slope and hydrological processes,
513 and also that thick sediment deposits at the beds of former supraglacial ponds are an
514 important additional control on the local variability of debris thickness. Surface debris appears
515 to be mobilized and transported by slope- and aspect-dependent sliding caused by sub-debris
516 melting, and most likely triggered by meltwater activity. Debris is redistributed from steep
517 slopes to shallow slopes and to ice-surface depressions that are often of hydrological origin.
518 However, the relationship between debris thickness and morphometric terrain parameters is
519 complex. While there is some apparent variation of debris thickness with slope and aspect,
520 whereby thinner debris caused by slope failure is more likely to occur on steeper slopes with
521 aspects that receive more abundant solar radiation, we find no meaningful variation with
522 curvature. This, combined with observations of slide-type debris morphology, suggests that
523 mass movement on the Ngozumpa glacier occurs on relatively short timescales and
524 predominantly by processes that occur at the limits of gravitational stability (e.g. Moore, 2017).
525 Slope stability modeling suggests that large areas of the glacier are potentially prone to failure,
526 and thus, as failure forms areas of thinner debris, that melting in these areas might be important
527 at the glacier scale.

528

529 *Data availability* Debris thickness data measured on Ngozumpa glacier will be made publicly
530 available on <https://zenodo.org/>

531 *Author contribution* LN, MM and HP contributed to field data collection. LN analyzed the debris
532 thickness distributions, performed melt modelling and led the preparation of the manuscript.



533 MM, with guidance from HP and IW, processed the GPR data, performed terrain analysis, and
534 slope stability modelling. All authors contributed to finalizing the manuscript.

535 *Competing interests* The authors declare that they have no conflict of interest.

536 *Acknowledgements* This research is supported by the Austrian Science Fund (FWF) projects
537 V309 and P28521 and the Austrian Space Applications Program of the Austrian Research
538 promotion agency (FFG) project 847999. M.M. is funded by NERC DTP grant number:
539 NE/L002507/1 and receives CASE funding from Reynolds International Ltd. HP was funded by a
540 British Antarctic Survey collaboration grant. The field team in Nepal was U Blumthaler, M
541 Chand, C del Gobbo, A Groos, A Lambrecht, C Mayer, H Pritchard, L Rieg and A Wirbel. C Klug
542 generated the DEM. Debris thicknesses data on Haut Glacier d’Arolla was collected by M
543 Carenzo, F Pellicciotti and L Peterson and provided by T Reid.



544 **References**

- 545 Arthern, R. J., Winebrenner, D. P. and Vaughan, D. G.: Antarctic snow accumulation mapped
546 using polarization of 4.3-cm wavelength microwave emission, *J. Geophys. Res. Atmos.*, 111(6),
547 1–10, doi:10.1029/2004JD005667, 2006.
- 548 Benn, D. I., Wiseman, S. and Hands, K. a.: Growth and drainage of supraglacial lakes on
549 debris-mantled Ngozumpa Glacier, Khumbu Himal, Nepal, *J. Glaciol.*, 47(159), 626–638,
550 doi:10.3189/172756501781831729, 2001.
- 551 Benn, D. I., Wiseman, S. and Warren, C. R.: Rapid growth of a supraglacial lake, Ngozumpa
552 Glacier, Khumbu Himal, Nepal, in *IAHS Publication*, vol. 264, pp. 177–185., 2000.
- 553 Benn, D., Thompson, S., Gulley, J., Mertes, J., Luckman, A. and Nicholson, L.: Structure and
554 evolution of the drainage system of a Himalayan debris-covered glacier, and its relationship
555 with patterns of mass loss, *Cryosphere*, 11(5), 2247–2264, doi:10.5194/tc-11-2247-2017, 2017.
- 556 Benn, D.I., Kirkbride, M., Owen, L.A. and Brazier, V.: Glaciated Valley Landsystems. In: D.J.A.
557 Evans (Ed), *Glacial Landsystems*. Arnold, 2003.
- 558 Bhatt, B. C. and Nakamura, K.: Characteristics of Monsoon Rainfall around the Himalayas
559 Revealed by TRMM Precipitation Radar, *Mon. Weather Rev.*, 133(1), 149–165,
560 doi:10.1175/MWR-2846.1, 2005.
- 561 Bolch, T., Buchroithner, M., Pieczonka, T. and Kunert, A.: Planimetric and volumetric glacier
562 changes in the Khumbu Himal, Nepal, since 1962 using Corona, Landsat TM and ASTER data, *J.*
563 *Glaciol.*, 54(187), 592–600, doi:10.3189/002214308786570782, 2008.
- 564 Buri, P., Pellicciotti, F., Steiner, J. F., Evan, S. and Immerzeel, W. W.: A grid-based model of
565 backwasting of supraglacial ice cliffs on debris-covered glaciers, *Ann. Glaciol.*, 57(71), in press,
566 doi:10.3189/2016AoG71A059, 2016.
- 567 Buri, P. and Pellicciotti, F.: Aspect controls the survival of ice cliffs on debris-covered glaciers,
568 *Proc. Natl. Acad. Sci.*, in revisio(Xx), 1–23, doi:10.1073/pnas.1713892115, 2018.
- 569 Conway, H. and Rasmussen, L. A.: Summer temperature profiles within supraglacial debris on
570 Khumbu Glacier, Nepal, in *IAHS Publication*, vol. 264, pp. 89–97, 2000.
- 571 Evatt, G. W., Abrahams, I. D., Heil, M., Mayer, C., Kingslake, J., Mitchell, S. L., Fowler, A. C. and
572 Clark, C. D.: Glacial melt under a porous debris layer, *J. Glaciol.*, 61(229), 825–836,
573 doi:10.3189/2015JoG14J235, 2015.
- 574 Fawcett, T.: An introduction to ROC analysis, *Pattern Recognit. Lett.*, 27(8), 861–874,
575 doi:10.1016/j.patrec.2005.10.010, 2006.
- 576 Finsterwalder, S. and lagally, M.: Die Nuevermessung des Suldenferers 1906 und dessen
577 Veränderungen in den letzten Jahrzehnten. *Zeitschrift für Gletscherkunde*, 13, 1-7, 1913.
- 578 Foster, L. a., Brock, B. W., Cutler, M. E. J. and Diotri, F.: A physically based method for estimating
579 supraglacial debris thickness from thermal band remote-sensing data, *J. Glaciol.*, 58(210), 677–
580 691, doi:10.3189/2012JoG11J194, 2012.



- 581 Gibson, M. J., Glasser, N. F., Quincey, D. J., Mayer, C., Rowan, A. V. and Irvine-Fynn, T. D. L.:
582 Temporal variations in supraglacial debris distribution on Baltoro Glacier, Karakoram between
583 2001 and 2012, *Geomorphology*, 295, 572–585, doi:10.1016/j.geomorph.2017.08.012, 2017.
- 584 Heimsath, A. M., Dietrichs, W. E., Nishiizuml, K. and Finkel, R. C.: The soil production function
585 and landscape equilibrium, *Nature*, 388(6640), 358–361, doi:10.1038/41056, 1997.
- 586 Herreid, S. and Pellicciotti, F.: Automated detection of ice cliffs within supraglacial debris cover,
587 *Cryosph. Discuss.*, (October), 1–33, doi:10.5194/tc-2017-205, 2017.
- 588 Hirschmüller, H.: Stereo processing by semiglobal matching and mutual information. *IEEE*
589 *Transaction on Pattern Analysis and Machine Intelligence*, 30 (2), 328–341, 2008.
- 590 Hock, R. & Noetzli, C.: Area melt and discharge modelling of Storglaciären, Sweden, *Ann. Glaciol.*,
591 24, 211–216, doi:10.1017/S0260305500012192, 1997
- 592 Ishikawa, M., Watanabe, T. and Nakamura, N.: Genetic differences of rock glaciers and the
593 discontinuous mountain permafrost zone in Kanchanjunga Himal, Eastern Nepal, *Permafr.*
594 *Periglac. Process.*, 12(3), 243–253, doi:10.1002/ppp.394, 2001.
- 595 Juen, M., Mayer, C., Lambrecht, A., Han, H. D. and Liu, S.: Impact of varying debris cover thickness
596 on ablation: a case study for Koxkar Glacier in the Tien Shan, *Cryosph.*, 8(2), 377–386,
597 doi:10.5194/tc-8-377-2014, 2014.
- 598 Kayastha, R. B., Takeuchi, Y., Nakawo, M. and Ageta, Y.: Practical prediction of ice melting
599 beneath various thickness of debris cover on Khumbu Glacier, Nepal, using a positive degree-
600 day factor, in *IAHS Publication*, vol. 264, pp. 71–81., 2000.
- 601 Kirkbride, M. P.: Ice-marginal geomorphology and Holocene expansion of debris-covered
602 Tasman Glacier, New Zealand, *IAHS Publ.*, (264), 211–217, 2000.
- 603 Kraaijenbrink, P. D. A., Bierkens, M. F. P., Lutz, A. F. and Immerzeel, W. W.: Impact of a global
604 temperature rise of 1.5 degrees Celsius on Asia's glaciers, *Nature*, 549(7671), 257–260,
605 doi:10.1038/nature23878, 2017.
- 606 Kurosaki, Y. and Kimura, F.: Relationship between Topography and Daytime Cloud Activity
607 around Tibetan Plateau., *J. Meteorol. Soc. Japan*, 80(6), 1339–1355, doi:10.2151/jmsj.80.1339,
608 2002.
- 609 Loomis, S.R.: Morphology and ablation processes on glacier ice. *Proceedings of the Association*
610 *of American Geographers*, 12: 88–92, 1970.
- 611 Mattson, L.E., Gardner, J.S. and Young, G.J.: Ablation on debris covered glaciers: an example from
612 the Rakhiot Glacier, Punjab, Himalaya. In: G.J. Young (Ed.), *Snow and glacier hydrology*. *IAHS-*
613 *IAHS Publication 218*, Wallingford, pp. 289–296, 1993
- 614 McCarthy, M., Pritchard, H. D., Willis, I. and King, E.: Ground-penetrating radar measurements of
615 debris thickness on Lirung Glacier, Nepal, *J. Glaciol.*, 63(239), 534–555,
616 doi:10.1017/jog.2017.18, 2017.



- 617 Mertes, J. R., Thompson, S. S., Booth, A. D., Gulley, J. D. and Benn, D. I.: A conceptual model of
618 supra-glacial lake formation on debris-covered glaciers based on GPR facies analysis, *Earth Surf.*
619 *Process. Landforms*, 42(6), 903–914, doi:10.1002/esp.4068, 2017.
- 620 Mihalcea, C., Brock, B. W., Diolaiuti, G., D'Agata, C., Citterio, M., Kirkbride, M. P., Cutler, M. E. J. and
621 Smiraglia, C.: Using ASTER satellite and ground-based surface temperature measurements to
622 derive supraglacial debris cover and thickness patterns on Miage Glacier (Mont Blanc Massif,
623 Italy), *Cold Reg. Sci. Technol.*, 52(3), 341–354, 2008.
- 624 Mihalcea, C., Mayer, C. and Diolaiuti, G.: Spatial distribution of debris thickness and melting from
625 remote-sensing and meteorological data, at debris-covered Baltoro glacier, Karakoram,
626 Pakistan, *Ann. Glaciol.*, 48, 49–57, 2008.
- 627 Mihalcea, C., Mayer, C., Diolaiuti, G., Lambrecht, A., Smiraglia, C. and Tartari, G.: Ice ablation and
628 meteorological conditions on the debris-covered area of Baltoro glacier, Karakoram, Pakistan,
629 *Ann. Glaciol.*, 43(1894), 292–300, 2006.
- 630 Miles, E. S., Pellicciotti, F., Willis, I. C., Steiner, J. F., Buri, P. and Arnold, N. S.: Refined energy-
631 balance modelling of a supraglacial pond, Langtang Khola, Nepal, *Ann. Glaciol.*, 57(71), 29–40,
632 doi:10.3189/2016AoG71A421, 2016.
- 633 Miles, K. E., Hubbard, B., Irvine-Fynn, T. D. L., Miles, E. S., Quincey, D. J. and Rowan, A. V.: Review
634 article: The hydrology of debris-covered glaciers; state of the science and future research
635 directions, *Cryosph. Discuss.*, 1–48, doi:10.5194/tc-2017-210, 2017.
- 636 Montgomery, D. R. and Dietrich, W. E.: A physically based model for the topographical control on
637 shallow landsliding, *Water Resour. Res.*, 30(4), 1153–1171, doi:10.1029/93WR02979, 1994.
- 638 Moore, P. L.: Stability of supraglacial debris, *Earth Surf. Process. Landforms*,
639 doi:10.1002/esp.4244, 2017.
- 640 Nicholson, L. I. and Benn, D. I.: Calculating ice melt beneath a debris layer using meteorological
641 data, *J. Glaciol.*, 52(178), 463–470, 2006.
- 642 Nicholson, L. I. and Benn, D. I.: Properties of natural supraglacial debris in relation to modelling
643 sub-debris ice ablation, *Earth Surf. Process. Landforms*, 38(5), 409–501, doi:10.1002/esp.3299,
644 2012.
- 645 Nicholson, L. I. and Mertes, J. R.: Thickness estimation of supraglacial debris above ice cliff
646 exposures using a high-resolution digital surface model derived from terrestrial photography, *J.*
647 *Glaciol.*, 1–10, doi:10.1017/jog.2017.68, 2017
- 648 .Nuimura, T., Fujita, K., Yamaguchi, S. and Sharma, R. R.: Elevation changes of glaciers revealed
649 by multitemporal digital elevation models calibrated by GPS survey in the Khumbu region,
650 Nepal Himalaya, 1992–2008, *J. Glaciol.*, 58(210), 648–656, doi:10.3189/2012JoG11J061, 2012
- 651 .Østrem, G.: Ice melting under a thin layer of moraine, and the existence of ice cores in moraine
652 ridges. *Geografiska Annaler*, 51(4): 228-230, 1959.
- 653 Pelletier, J. D. and Rasmussen, C.: Geomorphically based predictive mapping of soil thickness in
654 upland watersheds, *Water Resour. Res.*, 45(9), doi:10.1029/2008WR007319, 2009.



- 655 Quincey, D. J., Luckman, A. and Benn, D. I.: Quantification of Everest region glacier velocities
656 between 1992 and 2002, using satellite radar interferometry and feature tracking, *J. Glaciol.*,
657 55(192), 596–606, doi:10.3189/002214309789470987, 2009.
- 658 Reid, T. D. and Brock, B. W.: Assessing ice-cliff backwasting and its contribution to total ablation
659 of debris-covered Miage glacier, Mont Blanc massif, Italy, *J. Glaciol.*, 60(219), 3–13,
660 doi:10.3189/2014JG13J045, 2014.
- 661 Reid, T. D. and Brock, B. W.: An energy-balance model for debris-covered glaciers including heat
662 conduction through the debris layer, *J. Glaciol.*, 56(199), 903–916, 2010.
- 663 Reid, T. D., Carenzo, M., Pellicciotti, F. and Brock, B. W.: Including debris cover effects in a
664 distributed model of glacier ablation, *J. Geophys. Res.*, 117(D18), 1–15,
665 doi:10.1029/2012JD017795, 2012.
- 666 Rounce, D. R. and McKinney, D. C.: Debris thickness of glaciers in the Everest Area (Nepal
667 Himalaya) derived from satellite imagery using a nonlinear energy balance model, *Cryosph.*,
668 8(1), 1317–1329, doi:10.5194/tc-8-1317-2014, 2014.
- 669 Sakai, A., Takeuchi, N., Fujita, K. and Nakawo, M.: Role of supraglacial ponds in the ablation
670 process of a debris-covered glacier in the Nepal Himalayas, in *IAHS Publication*, vol. 265, pp.
671 119–132, 2000.
- 672 Schauwecker, S., Rohrer, M., Huggel, C., Kulkarni, A., Ramanathan, A. L., Salzmann, N., Stoffel, M.
673 and Brock, B. W.: Remotely sensed debris thickness mapping of Bara Shigri Glacier, Indian
674 Himalaya, *J. Glaciol.*, 61(228), 675–688, doi:10.3189/2015JG14J102, 2015.
- 675 Shea, J. M., Wagnon, P., Immerzeel, W. W., Biron, R., Brun, F. and Pellicciotti, F.: A comparative
676 high-altitude meteorological analysis from three catchments in the Nepalese Himalaya, *Int. J.*
677 *Water Resour. Dev.*, (May), 1–27, doi:10.1080/07900627.2015.1020417, 2015.
- 678 Thompson, S. S., Benn, D. I., Dennis, K. and Luckman, A.: A rapidly growing moraine-dammed
679 glacial lake on Ngozumpa Glacier, Nepal, *Geomorphology*, 145–146, 1–11,
680 doi:10.1016/j.geomorph.2011.08.015, 2012.
- 681 Thompson, S. S., Benn, D. I., Mertes, J. and Luckman, A.: Stagnation and mass loss on a Himalayan
682 debris-covered glacier: Processes, patterns and rates, *J. Glaciol.*, 62(233), 467–485,
683 doi:10.1017/jog.2016.37, 2016.
- 684 Wagnon, P., Vincent, C., Arnaud, Y., Berthier, E., Vuillermoz, E., Gruber, S., Ménégoz, M., Gilbert,
685 A., Dumont, M., Shea, J. M., Stumm, D. and Pokhrel, B. K.: Seasonal and annual mass balances of
686 Mera and Pokalde glaciers (Nepal Himalaya) since 2007, *Cryosphere*, 7(6), 1769–1786,
687 doi:10.5194/tc-7-1769-2013, 2013.
- 688 Watson, C. S., Quincey, D. J., Carrivick, J. L. and Smith, M. W. M. W. M. W. M. W. M. W.: The
689 dynamics of supraglacial ponds in the Everest region, central Himalaya, *Glob. Planet. Change*,
690 142, 14–27, doi:10.1016/j.gloplacha.2016.04.008, 2016.
- 691 Zhang, Y., Fujita, K., Liu, S., Liu, Q. and Nuimura, T.: Distribution of debris thickness and its effect
692 on ice melt at Hailuoguo glacier, southeastern Tibetan Plateau, using in situ surveys and ASTER
693 imagery, *J. Glaciol.*, 57(206), 1147–1157, doi:10.3189/002214311798843331, 2011.



694 *Table 1: Details of processing steps applied to radargrams, in order of use from left to right, using*
 695 *REFLEXW software. T is the period of the transmitted signal, t is two-way travel time and f is*
 696 *operating frequency.*

operating frequency (MHz)	plateau declip	DC shift	dewow (ns)	align first breaks	timezero correct (s)	back-ground removal	band-pass filter	gain
200	whole profile	whole profile	1.5T (7.5)	whole profile	7.6719e ⁻¹⁰	whole profile	0.25f, 0.5f, 1.5f, 3f	divergence compensation (scaling 0.1t)
600			1.5T (7.5)		3.2022e ⁻¹⁰			

697



Table 2: Statistics of sampled debris thickness variability measured at different locations on Ngozumpa, and other, glaciers by a range of methods.

site	glacier	method	source	n	m	sample/m	mean	mode	skewness	kurtosis	25%	75%	min	max
Ngozumpa 1km	Ngozumpa	GPR*	this study (Margin)	13983	238	58.75	3.33	2.19	0.48	1.84	2.23	4.35	1.74	5.96
Ngozumpa 1km	Ngozumpa	theodolite	Nicholson and Benn, 2012 (upper)	92	460	0.20	1.65	1.87	0.87	3.76	1.05	2.14	0.12	4.36
Ngozumpa 3km	Ngozumpa	GPR*	this study (Gokyo)	130926	3301	39.66	1.95	1.33	1.06	3.60	0.93	2.71	0.18	7.34
Ngozumpa 3km	Ngozumpa	SIM-MVS	Nicholson and Mertes, 2017	1011	980	1.00	1.82	0.75	1.33	4.13	0.73	2.46	0.02	7.62
Ngozumpa 7km	Ngozumpa	theodolite*	Nicholson and Benn, 2012 (lower)	143	715	0.20	0.59	0.09	1.93	8.27	0.25	0.92	0.09	3.22
Lirung	Lirung	GPR points	McCarthy and others, 2017	6198	354	17.51	0.66	0.39	1.07	3.24	0.32	0.93	0.11	2.30
Suldenferner	Sulden	GPR	del Gobbo, 2017	61136	1000	61.14	0.32	0.29	0.07	3.39	0.26	0.38	0.00	0.74
Suldenferner	Sulden	excavation	del Gobbo, 2017	101	10100	0.01	0.14	0.10	2.05	7.49	0.06	0.16	0.00	0.67
Arolla	Arolla	excavation	Reid and others, 2012*	488	976	0.50	0.07	0.01	6.29	68.86	0.02	0.08	0.01	1.50

* Data used in ablation modelling in this study
 † Data from the medial moraine only, excluding measurements of patchy debris (< 0.01 m in thickness)

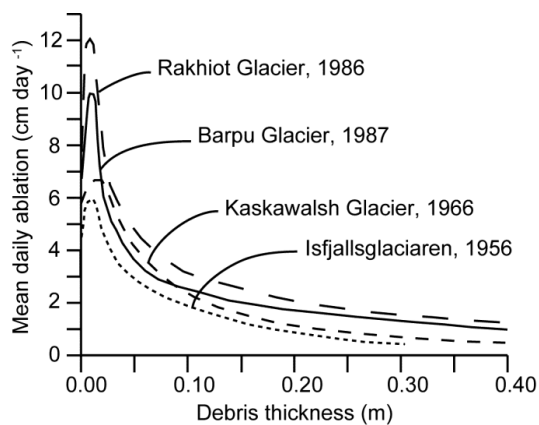


Fig. 1: Examples of the relationships between supraglacial debris thickness and underlying ice ablation rate at different glacier sites, redrawn from Mattson et al. (1993). The exact form of this relationship at each site varies with prevailing meteorological conditions and debris properties, but its general character is preserved.

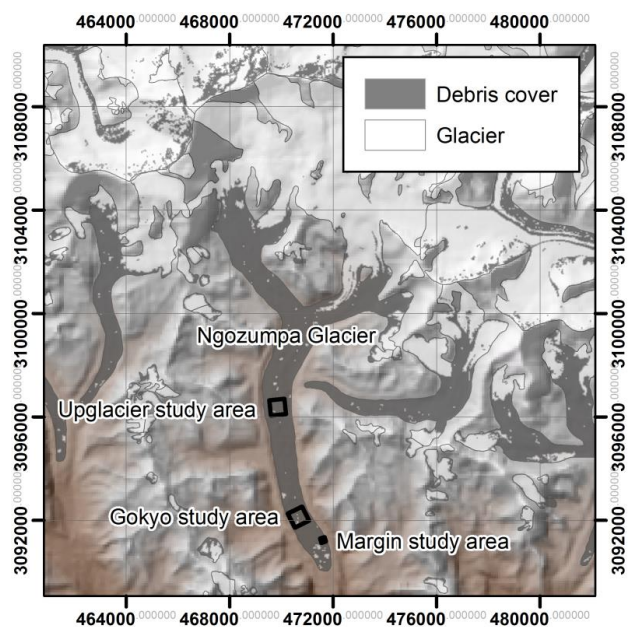


Fig. 2: (a) Ngozumpa glacier showing the key study areas, ~7, 2 and 1 km from the glacier terminus (b) Photograph showing example hummocky terrain in the upglacier study area – note the people for scale in the bottom right corner. Photo credit H. Pritchard.

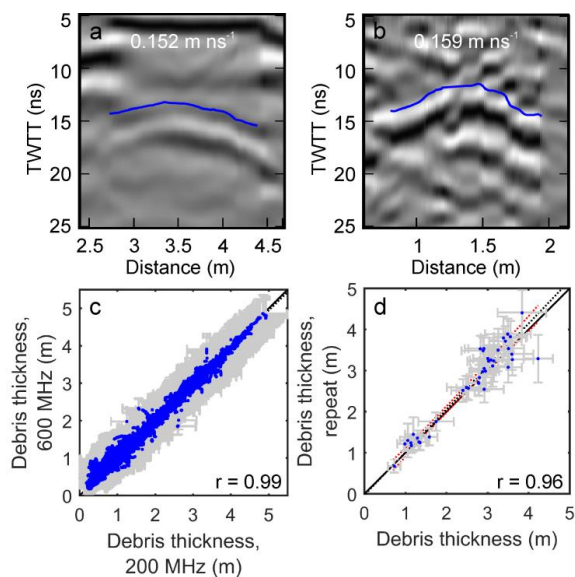


Fig. 3: Reflector used to identify signal velocity on Ngozumpa glacier in (a) fine-grained sediments and (b) coarse-grained sediments. Comparison of picked debris ice interface depths sampled simultaneously with different frequencies (c) and at transect intersection points (d).

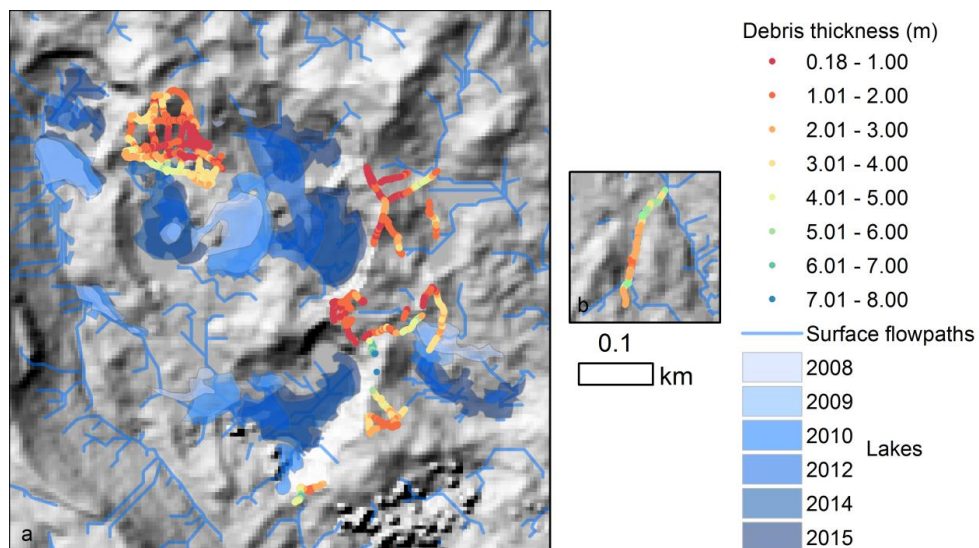


Fig. 4: Overview map of GPR debris thickness sampled on Ngozumpa glacier in 2016 overlain on the hillshade from the Pleiades DTM, recent surface pond evolution, and surface flow paths for the Gokyo(a) and Margin (b) study areas (Fig. 2).

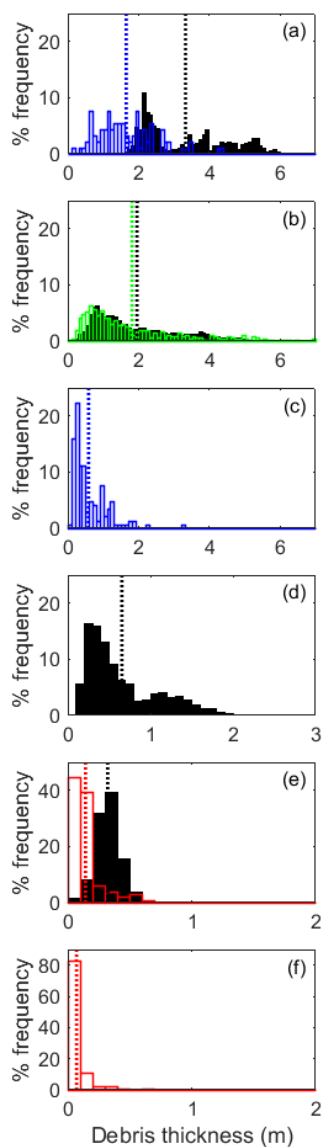


Fig. 5: Percentage frequency histograms of debris thickness (h_d) in 0.05 m intervals at (a) the lower Ngozumpa about 1 km from the terminus; (b) Gokyo area of Ngozumpa, about 2 km from the terminus; (c) upper Ngozumpa, about 7 km from the terminus; (d) over the lower tongue of Lirung glacier in central Nepal; (e) across the debris covered ablation area of Suldenerferner/Ghiacciaio de Solda in the Italian Alps; (f) the medial moraine of Haut Glacier d'Arolla in the Swiss Alps. Measurement methods are GPR (black); theodolite surveys (blue); Structure from Motion (SfM-MVS) photographic terrain model (green) and excavation of pits (red). Note that axes vary between sites, and summary statistics of these distributions are in Table 2.

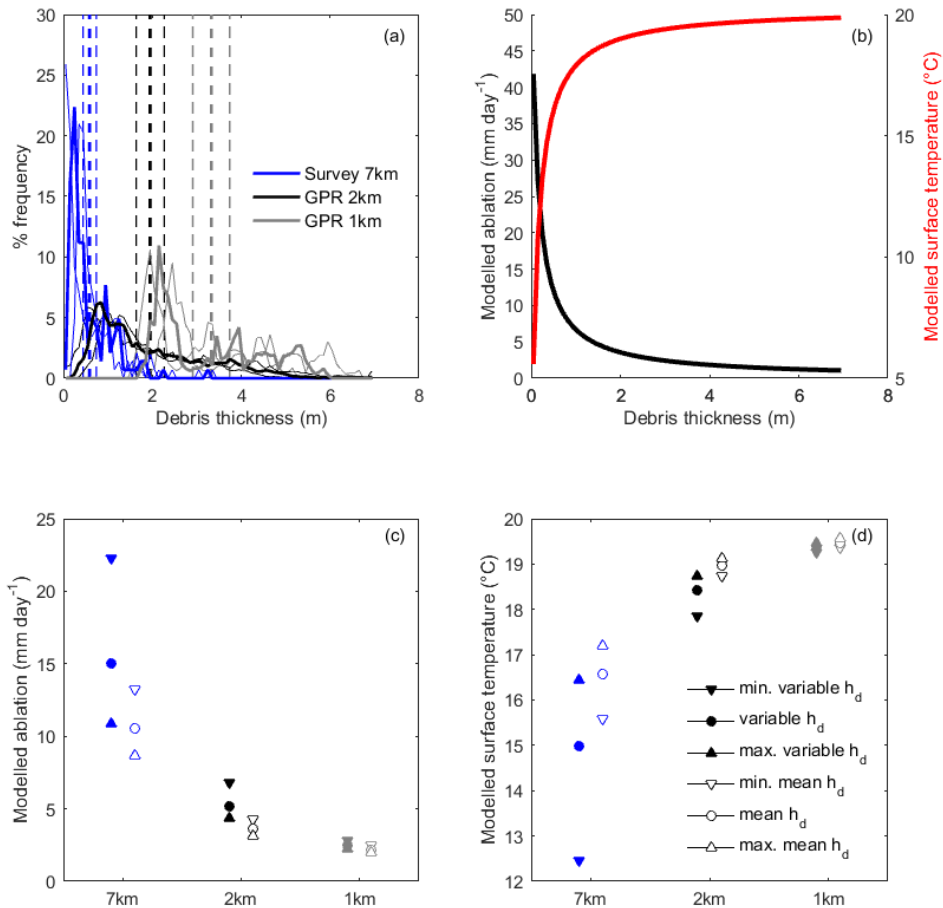


Fig. 6: (a) Percentage frequency distributions from three locations on Ngozumpa glacier, showing the mean debris thickness at each site in dotted vertical lines: 3.33, 1.95 and 0.59 m thick respectively at 1, 2 and 7 km from the terminus. Thinner lines show the values for the maximum and minimum debris thickness conditions calculated from the limits of the individual debris thickness errors. (b) Modelled Østrem curve and surface temperature for mean August conditions. (c) Comparison of modelled ablation for different representations of the debris thickness at each site. (d) Comparison of modelled surface temperature for different representations of the debris thickness at each site.

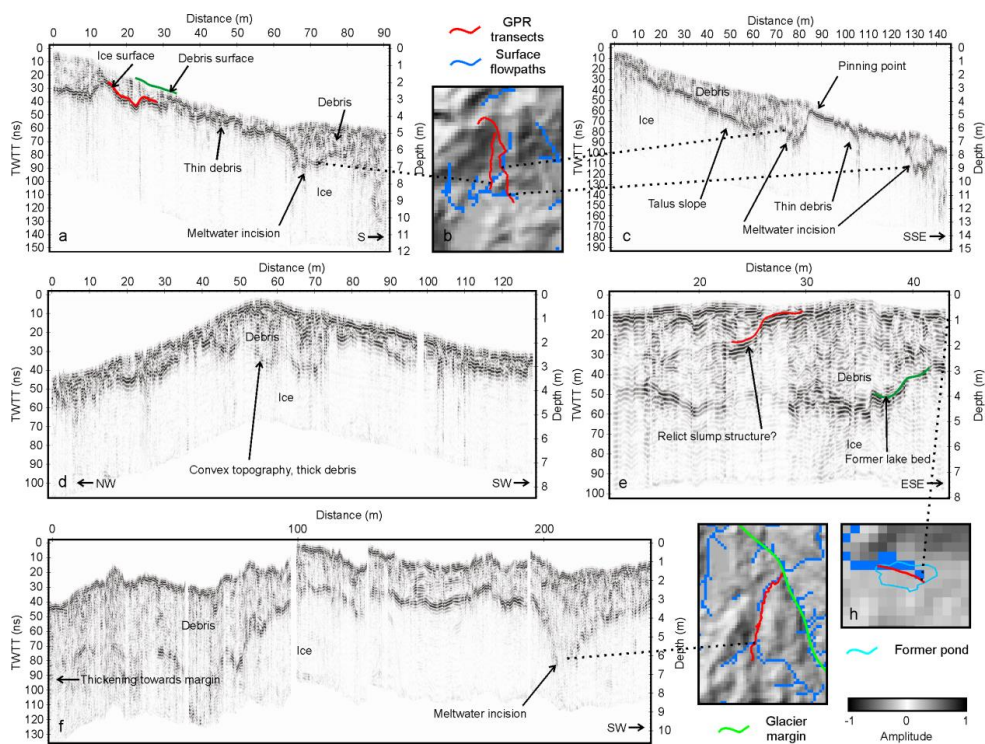


Fig. 7: Example radargrams showing debris thickness variability and internal structures in relation to local topography and surface meltwater flow pathways.

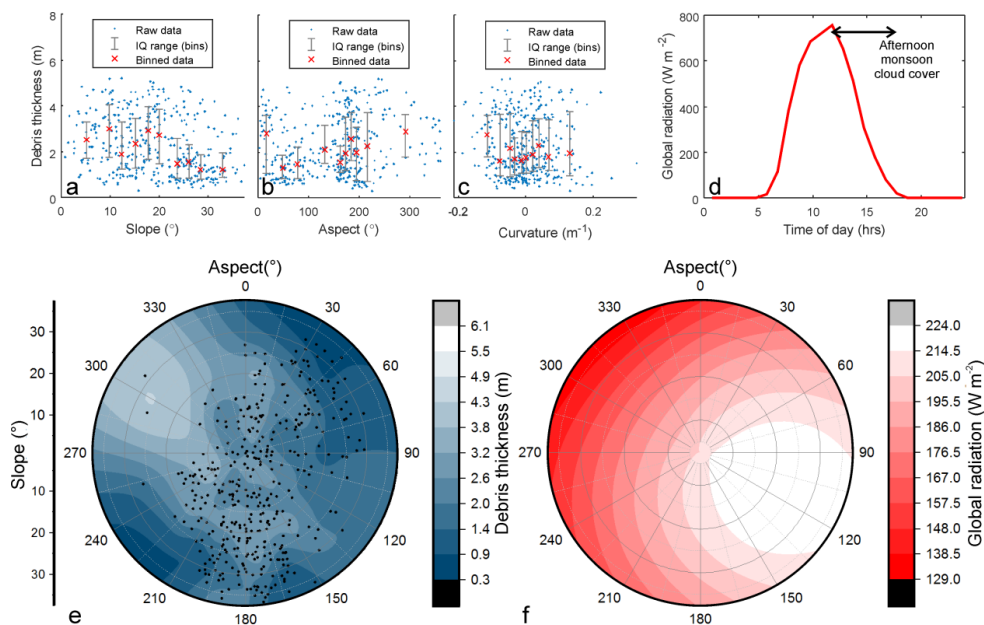


Fig. 8: Summary of relationships between measured debris thickness and terrain properties: (a) debris thickness related to local slope angle; (b) debris thickness related to local slope aspect; (c) debris thickness related to curvature (d) August global radiation data collected on the glacier during the survey period; (e) hemispheric plot of debris thickness (showing sub-sampled data points) related to slope angle and aspect; (f) hemisphere plot of August global radiation, distributed on surfaces of different slope and aspect following Hock and Noezli (1997).

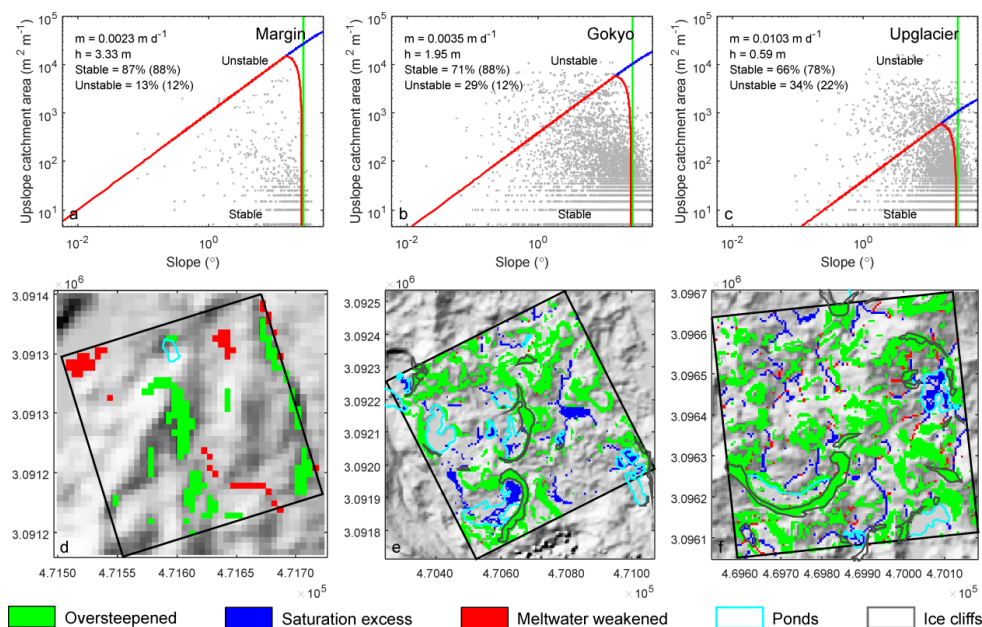


Figure 9: Results of debris stability modelling: Upslope catchment area as a function of slope angle for the three study areas (a-c); points falling above or to the right of the plotted lines are unstable. Percentage area stability/instability values are given with lakes and ice cliffs included, and in brackets with lakes and ice cliffs excluded. Maps of spatial distribution of terrain stability classifications for each study area (d-e), highlighting ponds and ice cliffs.